electronics

MDPI

Article

Impact of Phase Perturbations on Power Combining Performance of RTD Oscillator Arrays Based on an Equivalent Circuit Model

Liyuan Yu *, Guang Yang, Hongwei Wang, Yi Liu, Sirui Yao and Haotian Zhu

School of Electronics and Information Engineering, Tiangong University, Tianjin 300387, China; 19290700692@163.com (G.Y.); 19188337996@163.com (H.W.); 18838157350@163.com (Y.L.); yaosiri@163.com (S.Y.); zht020621@163.com (H.Z.)
* Correspondence: yuliyuan@tiangong.edu.cn; Tel.: +86-159-0031-2715

Abstract

An equivalent-circuit model is developed to investigate the effects of fabrication-induced phase perturbations on coherent power combining in terahertz resonant tunneling diode (RTD) oscillator arrays. The resonant tunneling and residual excess currents are represented by two nonlinear voltage-controlled current sources, while the slot antenna is modeled as an equivalent RLC resonant network. Fabrication-induced phase perturbations are modeled by introducing controlled variations in the intrinsic capacitance of individual oscillator units. A GaInAs/AlAs RTD oscillator operating at 220 GHz delivers an output power of 74.56 μW, and its simulated current–voltage characteristics agree well with experimental data. The model is subsequently extended to 1 × 2, 2 × 2, and 4 × 4 arrays, yielding output powers of 140.67, 269.71, and 1053.39 μW and combining efficiencies of 94.33%, 90.43%, and 88.30%, respectively. For the 2 × 2 array, increasing the phase perturbation from 0° to 2° reduces the output power from 269.71 μW to 255.32 μW. The proposed model enables the analysis of phase perturbations arising from fabrication-induced variations in individual RTD oscillator units and provides a theoretical basis for the design and optimization of scalable, high-efficiency terahertz RTD oscillator arrays.

Keywords: terahertz oscillator; resonant tunneling diode; coupled array; equivalent circuit; phase perturbation

1. Introduction

Terahertz (THz) technology offers unique advantages and broad application prospects across numerous fields [1]. Among its critical components, the THz source, which generates terahertz radiation, forms the cornerstone of any THz system. Currently, THz sources are generally categorized into optical sources based on laser technology, vacuum electronic devices, and solid-state electronic sources. Among these, solid-state electronic sources, particularly resonant tunneling diodes (RTD), have attracted considerable research interest due to their ability to operate at room temperature, compact footprint, and compatibility with integration processes [2], positioning RTD as a highly promising candidate for THz generation [3].

Leveraging their negative differential resistance (NDR) characteristic, RTD can sustain fundamental oscillations from hundreds of gigahertz up to the terahertz range at room temperature. In 2008, Asada et al. established a comprehensive equivalent circuit model for RTD oscillators, identifying tunneling time and transit time as the primary factors limiting their high-frequency performance [4]. In 2009, Suzuki et al. achieved 831 GHz fundamental

Check for updates

Academic Editor: Toshifumi Moriyama

Received: 18 September 2026
Revised: 2 November 2026
Accepted: 3 November 2026
Published: 5 November 2026

Copyright: © 2026 by the authors. Licensee MDPI, Basel, Switzerland. This article is an open access article distributed under the terms and conditions of the Creative Commons Attribution (CC BY) license.

oscillation at room temperature by optimizing the collector spacer thickness and emitter doping concentration [5]. In 2013, Asada et al. integrated an offset-feed structure with a RTD array, realizing a coherent power-combined output of 610 μW at 620 GHz [6]. In 2019, Kasagi et al. reported a large-scale RTD oscillator array with an output of 730 μW near 1 THz [7]. In 2022, Suzuki et al. demonstrated continuous phase tuning at 380 GHz in injection-locked RTD oscillators using a heterodyne phase detection system [8].

In terahertz oscillator arrays, achieving efficient spatial power combining ideally requires all array elements to maintain both frequency and phase coherence. However, in practice, packaging effects such as gold wire bonding can shift the RTD oscillation frequency [9], while device dimension variations, impedance mismatch, fabrication tolerances, and bias fluctuations can all degrade oscillation consistency [10], inevitably introducing random phase perturbations among individual oscillators. Such phase mismatches degrade the overall phase coherence of the array, thereby reducing the total output power and power combining efficiency. Therefore, a systematic investigation into the effects of individual element phase perturbations on total array output power is essential, as it clarifies the physical mechanisms of combining efficiency degradation, reveals the phase consistency–array size relationship, and provides theoretical support for terahertz source and phased-array system design. Regarding phase control, Asada theoretically analyzed subharmonic injection locking in RTD oscillators [11]. However, this approach relies on an external injection source and does not address array-level phase synchronization. In contrast, our proposed model achieves continuous phase tuning by adjusting the intrinsic capacitance of adjacent coupling units, providing a simpler and more scalable solution for array-level synchronization. Furthermore, while Meng et al. demonstrated high-power coherent emission in an 11-element linear array [12], the effect of fabrication-induced phase perturbations on combining efficiency was not systematically quantified. Our work bridges this gap by quantitatively revealing the relationship between phase perturbations (0° to 2°) and power combining efficiency in 2 × 2 and 4 × 4 arrays. These comparisons clearly demonstrate the novelty of our work: a unified framework for device-level and array-level analysis, a simple intrinsic-capacitance-based phase tuning mechanism, and quantitative insights into fabrication-induced phase perturbations.

This paper presents an equivalent circuit modeling approach for RTD-based terahertz oscillator units and arrays, with a focus on the effect of phase perturbations on array power combining. The RTD oscillator model, which incorporates a nonlinear voltage-controlled current source and an RLC resonant network representing the slot antenna, is developed to enable time-domain transient and output power analyses. By adjusting the intrinsic capacitance in the equivalent circuit, the model achieves continuous phase tuning among the array units. Fine control of the phase perturbation, introduced via variations in active layer thickness, is used to assess its impact on power combining efficiency. Using this framework, the power combining performance of both a 220 GHz 2 × 2 array and a 4 × 4 extended array is analyzed, providing guidance for the design of high-power RTD-based THz arrays.

2. Materials and Methods

2.1. Equivalent Circuit Model of a Single RTD Oscillator

In this section, an equivalent-circuit model for a single GaInAs/AlAs resonant tunneling diode (RTD) oscillator is constructed to serve as the fundamental building block for subsequent array-level simulations. The RTD current density is considered to consist of two

components: the resonant tunneling current J_{RT} and the residual excess current J_{EX} [13]. The total current density can be described as follows:

$$J = J_{RT} + J_{EX} \tag{1}$$

According to the current–voltage equation proposed by J.N.Schulman et al. [14], the resonant tunneling current J_{RT} and the residual excess current J_{EX} can be expressed as follows:

$$J_{RT} = A \ln\left[\frac{1+e^{(B-C+n_1V)e/KT}}{1+e^{(B-C-n_1V)e/KT}}\right] \times \left[\frac{\pi}{2} + \tan^{-1}\left(\frac{C-n_1V}{D}\right)\right] \tag{2}$$

$$J_{EX} = H\left(e^{n_2eV/KT} - 1\right) \tag{3}$$

The model parameters are extracted based on the fitting analysis of the GaAs-RTD current–voltage characteristics reported in [15], as follows: $A = 4.68 \times 10^{-4}$, $B = 1.5168$, $C = 1.62487$, $D = 0.140$, $n_1 = 1.863$, $H = 2.75 \times 10^{-8}$, $n_2 = 0.162$. The corresponding functions are given as follows:

$$J_{RT} = 4.68 \times 10^{-4} \times \ln\left(\frac{1+e^{6.9V-4}}{1+e^{-6.9V-4}}\right) \times \left[1.57 + \tan^{-1}(11.6 - 1.29V)\right] \tag{4}$$

$$J_{EX} = 2.75 \times 10^{-8} \times (e^{6V} - 1) \tag{5}$$

Based on the above equations, an equivalent-circuit model of the RTD is established. In this model, the resonant tunneling current J_{RT} and residual excess current J_{EX} are represented by two nonlinear voltage-controlled current sources, G_1 and G_2, respectively. The voltage difference between the input terminals U_1 and U_2 of the two controlled current sources is defined as the voltage V. The intrinsic capacitance C_d is modeled by combining the barrier capacitance C_{rtd} and the depletion-layer capacitance C_0 of the RTD, as commonly adopted in equivalent-circuit construction [16]. With a RTD mesa area of 1.8×1.8 μm^2, the barrier capacitance C_{rtd} is calculated to be 3.24 fF. For an active layer thickness of 7.5 nm, the depletion-layer capacitance C_0 is 41.63 fF. Therefore, the intrinsic capacitance C_d is determined to be 44.87 fF. The negative differential resistance R_d of the RTD is set to 77.5 Ω, as has been considered in related capacitance studies [17].

The antenna structure of the oscillator is implemented as a slot antenna, whose resonant behavior is represented by an equivalent RLC circuit. Using a similar parameter extraction method and the oscillation frequency of 220 GHz, the equivalent antenna parameters are obtained as $C_{ant} = 3.31$ fF, $L_{ant} = 10.71$ pH, and $R_{ant} = 265$ Ω [18]. For the subsequent circuit simulations, the parameters C_d and C_{ant} are initially determined based on the target operating frequency of 220 GHz. It should be noted that the actual oscillation frequency is determined by the complete resonant tank rather than the isolated antenna. At the small-signal level used to extract the resonance, the DC bias terminal is treated as AC ground; after reducing the internal device node to the output port, the RTD intrinsic capacitance C_d contributes to the same port capacitance as C_{ant}, together with L_{ant}, from which the network settles at the operating point [19]. The theoretical resonant frequency is approximately 221.7 GHz, which agrees well with our simulated 220 GHz operating frequency. In addition, a 1 Ω series resistance Rs is introduced to account for the RTD series resistance loss and improve the numerical stability and convergence of the simulation [20]. The corresponding single-RTD oscillator equivalent-circuit model is shown in Figure 1. The intrinsic capacitance C_d is further employed as the tuning parameter to introduce controlled phase perturbations among oscillator units, which enables quantitative investigation of phase mismatch effects on array synchronization and power combining performance.

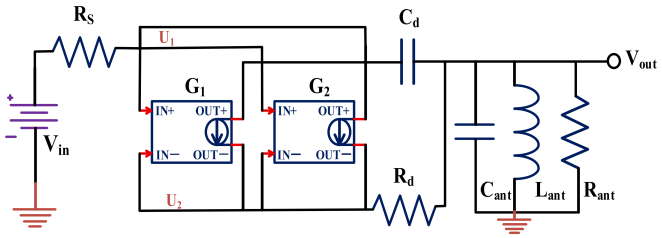


Figure 1. Single RTD oscillator model. The red arrow indicates the input terminals of the nonlinear voltage-controlled current sources.

2.2. Equivalent Circuit Model of the RTD Oscillator Array

Building upon the validated single-oscillator model presented in Section 2.1, this subsection extends the circuit architecture to construct coupled RTD oscillator array models for coherent power-combining analysis. Based on the direct-coupling configuration of array elements through transmission lines [21], a 2 × 2 RTD oscillator array model is first constructed, as shown in Figure 2. In this model, the equivalent nonlinear voltage-controlled current sources of the four RTDs are connected through coupling resistors and biased by a common DC voltage source. Each oscillator unit is implemented in a modular form, where each RTO block contains three terminals: VDD, GND, and an output node (OUT). The VDD terminal corresponds to the input terminal V_{in} in the single-oscillator circuit, serving as the DC bias input for each oscillator unit. The overall array output signal is extracted from V_{out}, which is located at the midpoint of the equivalent resistance of the transmission-line network.

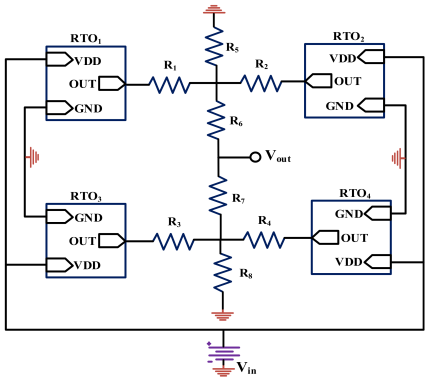


Figure 2. A 2 × 2 oscillator array circuit model.

In the proposed equivalent-circuit model, the coupling line is represented in a simplified manner by an equivalent resistor. At 220 GHz, the coupling-interconnect length adopted here is $L = 180$ μm; with an effective permittivity $\varepsilon_{eff} = 2.50$, the guided wavelength is approximately $\lambda_g \approx 0.86$ mm, the electrical length is roughly $\theta = 360° \cdot L/\lambda_g \approx 75°$ (about 1.31 rad), and the propagation delay is on the order of 0.95 ps. Within this equivalent-circuit framework, the lumped resistor may be regarded as a simplified phenomenological description of the effective coupling between adjacent RTD oscillator units, rather than a complete distributed microstrip model. To thoroughly validate the effectiveness of this approximation in capturing phase-perturbation sensitivity, a controlled comparison against a distributed transmission-line model is detailed in Section 3.4. Furthermore, the lumped-resistor model is deliberately adopted to simplify the circuit topology and facilitate the analysis of larger-scale arrays, thereby mitigating the risk of simulation non-convergence associated with implementing distributed transmission lines in every branch. Across the 2 × 2, 4 × 4, and larger-scale arrays, this simplified treatment is applied consistently to simplify the equivalent-circuit topology. This allows the influence of phase perturbations

on power loss and combining efficiency to be effectively examined at the circuit level. While this model primarily captures the conductor loss, the finer distributed propagation phases and frequency-dependent effects are not fully reproduced here. Therefore, future work will focus on full-wave electromagnetic simulations to further refine these aspects. Nevertheless, the present framework provides a reliable and scalable approach to analyze fabrication-induced phase perturbations and their relationship with array scales.

The equivalent resistance R_{couple} of the coupling line is composed of two components: the conductor loss resistance R_{cond} and the radiation/matching loss resistance R_{rad}, with R_{rad} taken as 36 Ω [22]. The conductor loss resistance R_{cond} can be calculated as follows:

$$R_{cond} = \frac{\rho \cdot L}{w \cdot \delta} \tag{6}$$

Assuming Au as the equivalent conductor material of the coupling line, with a resistivity of 2.4×10^{-8} Ω·m, the skin depth δ of Au at 220 GHz is calculated to be approximately 0.17 μm. With a length-to-width ratio of 18 for the coupling line, the conductor loss resistance R_{cond} is calculated to be approximately 2.6 Ω using Equation (6). Therefore, the equivalent resistance of the coupling line is determined to be 38.6 Ω. This value is considerably lower than the equivalent resistance of the slot antenna, satisfying the negative-resistance start-up condition of the RTD oscillator.

For the quantitative evaluation of the array performance, the output power and power combining efficiency are defined as follows. It should be clarified that R_d represents the internal active-region resistance and R_{ant} represents the antenna load; these two are not physically connected as a simple parallel branch at the output node. However, due to the high-frequency coupling in the equivalent circuit, the voltage swing at the output node is largely shared across both the device and the antenna. The reported output power P_{out} represents the total AC oscillation power of the active circuit, which is the superposition of the internal power dissipated by the device P_{Rd} and the power delivered to the antenna load P_{Rant}. The steady-state portion of $v_{out}(t)$ is obtained via transient analysis and transformed by a Fourier transform; the 220 GHz fundamental peak amplitude V_{peak} is read under the peak-to-effective convention $V_{peak} = \sqrt{2} \cdot V_{eff}$, where V_{eff} is the effective voltage of this fundamental. The total steady-state average output power is therefore expressed as a summation:

$$P_{out} = P_{R_d} + P_{R_{ant}} \tag{7}$$

where V_{eff} is the effective voltage of the isolated 220 GHz fundamental component, P_{Rd} and P_{Rant} denote the steady-state average power dissipated in the internal device resistance R_d and the antenna load R_{ant}, respectively, and P_{out} is the resulting total AC oscillation power evaluated from the 220 GHz fundamental spectral peak. For an $N \times N$ oscillator array (N = units per side), the power combining efficiency η is defined as:

$$\eta = \frac{Parray}{N^2 \cdot Psingle} \times 100\% \tag{8}$$

where P_{array} is the total output power of the array extracted from the spectrum, P_{single} is the output power of a single oscillator unit, and N denotes the number of units on each side, so that the total number of elements is N^2.

Based on the 2 × 2 oscillator array model, the array architecture is extended using the same coupling scheme, where each 2 × 2 subarray is regarded as a basic unit. Each subarray is biased by an independent DC source and interconnected through its central output node. A 4 × 4 RTD oscillator array model is subsequently constructed, as shown in Figure 3. This modular coupling strategy demonstrates good scalability and can be readily extended to larger array configurations.

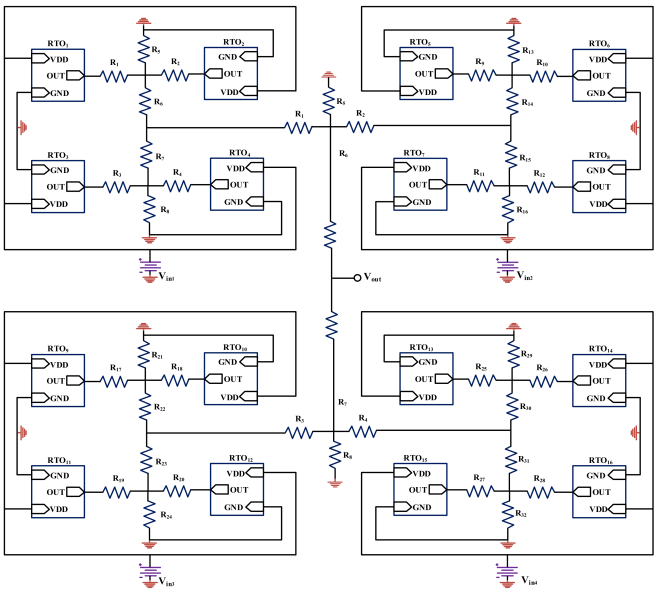


Figure 3. A 4 × 4 oscillator array model.

3. Results and Discussion

3.1. Equivalent Circuit Simulation

Prior to investigating array-level power-combining behaviors, DC and transient circuit simulations are carried out to verify the electrical and oscillation performance of the proposed single-RTD oscillator model. The simulated current–voltage (I–V) characteristic of the device is first obtained via DC analysis, as shown in Figure 4. The negative differential resistance characteristic of the RTD model is observed, with the NDR region extending from 0.95 V to 1.1 V. The peak current and the valley current are determined to be 1.74 mA and 0.51 mA, respectively, yielding a peak-to-valley current ratio (PVCR) of 3.4.

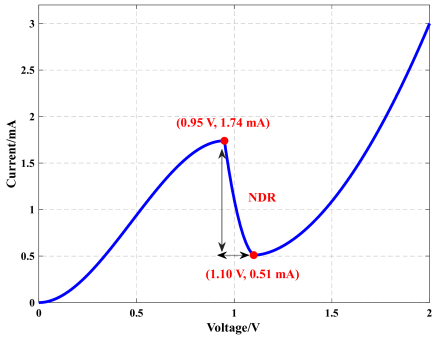


Figure 4. I–V characteristic curve of the RTD model.

Transient simulation is performed using the proposed single-oscillator model under a DC bias voltage of 1 V. The simulated time-domain waveform of the RTD oscillator is shown in Figure 5. The oscillator exhibits an oscillation period of 4.55 ps and a voltage amplitude of 93.47 mV. Self-sustained oscillation starts at approximately 190 ps and reaches a steady state at around 300 ps. In the steady-state region, the output waveform maintains a constant amplitude and uniform oscillation period without observable attenuation. These results demonstrate that the proposed model accurately captures the startup dynamics and steady-state oscillation characteristics of the RTD oscillator, validating its suitability for further analysis of RTD-based terahertz oscillator arrays. Therefore, the proposed oscillator model provides a reliable foundation for investigating phase synchronization and coherent power combining characteristics in RTD oscillator arrays.

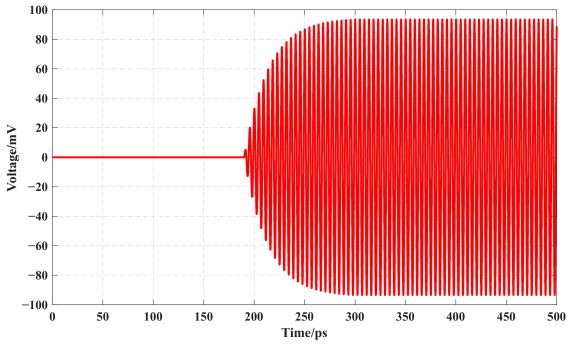


Figure 5. Oscillation waveform diagram of a single RTD oscillator.

The power spectrum of the single RTD oscillator is obtained through a Fourier transform. As shown in Figure 6, a dominant spectral peak appears at 220 GHz, demonstrating that the oscillator achieves stable fundamental oscillation at this frequency with an output power of 74.56 μW. Based on the theoretical power superposition, the calculated total AC power yields approximately 72.9 μW. The minor discrepancy between this theoretical value and the simulated extracted power of 74.56 μW is primarily attributed to the frequency resolution and numerical truncation errors inherent in the FFT spectral extraction process, which confirms the consistency and reliability of our equivalent circuit model. In addition to the fundamental component, several weak spectral peaks are observed, which are attributed to the second- and third-order harmonic components, respectively. The obtained oscillation frequency and output power are consistent with the design target, further validating the effectiveness of the proposed RTD oscillator model.

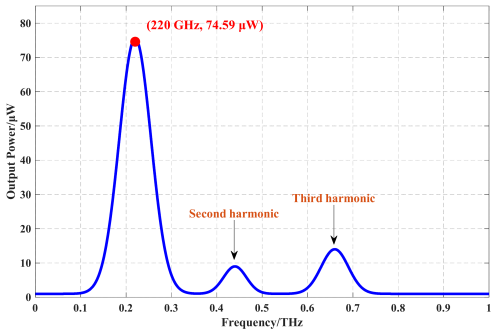


Figure 6. Power spectrum of a single RTD oscillator.

3.2. Array Output Power Simulation

With the single-oscillator model fully validated in Section 3.1, the equivalent-circuit framework is now applied to analyze the output-power characteristics of RTD oscillator arrays. The simulated output-power variation against oscillation frequency for the 2 × 2 array is presented in Figure 7. Each frequency point is obtained from DC operating-point analysis: the RTD mesa area (determining C_d) and the antenna RLC parameters are adjusted to satisfy the resonance condition at that frequency, while the circuit composition and the inter-unit coupling relationship remain unchanged. Within the frequency range from 200 GHz to 400 GHz, the output power increases monotonically with increasing frequency. A relatively flat region with the maximum output power is observed between 400 GHz and 700 GHz, whereas the output power decreases rapidly beyond 700 GHz. The simulated results and the corresponding fitted curve show good agreement with the experimental results of RTD oscillators [23].

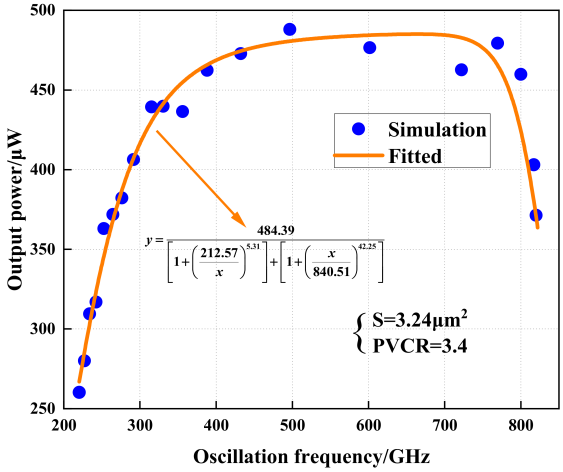


Figure 7. Curve of output power versus oscillation frequency for the 2 × 2 array oscillator.

Figure 8 presents the output power characteristics of RTD oscillator arrays with different array sizes. The simulation results show that the single RTD oscillator unit achieves an output power of 74.56 μW. The 1 × 2 oscillator array increases the output power to 140.67 μW, corresponding to a power combining efficiency of 94.33%, while the 2 × 2 oscillator array achieves an output power of 269.71 μW with a combining efficiency of 90.43%, and the 4 × 4 array delivers 1053.39 μW with a combining efficiency of 88.30%. As the number of array elements increases, additional ohmic losses are introduced in the array interconnection network, resulting in a slight reduction in the combining efficiency. These results provide a baseline for evaluating the degradation of coherent power combining efficiency under phase perturbations.

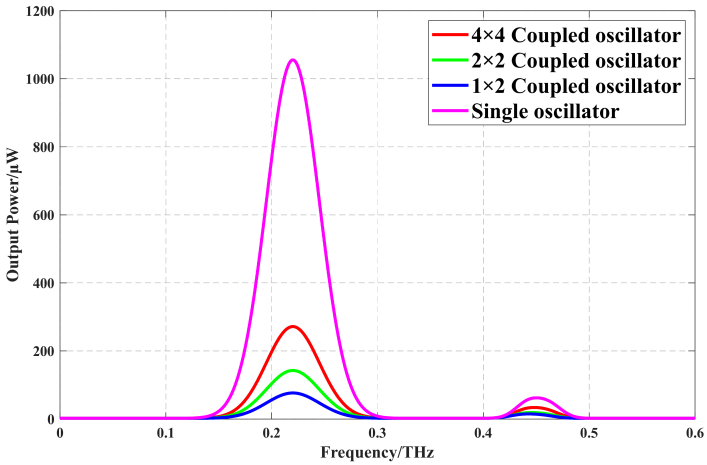


Figure 8. Power spectra of RTD oscillators with different array scales.

3.3. Phase Tuning of the Array Based on the Equivalent Circuit Model

To quantitatively study phase-mismatch effects induced by fabrication deviations, a phase-tuning method for array elements is implemented within the established equivalent-circuit framework. Phase perturbations between individual oscillator units are realized by adjusting the intrinsic capacitance C_d of each oscillator cell, where C_d is composed of the barrier capacitance C_{rtd} and the depletion-layer capacitance C_0, as shown in Figure 1. Although variation in C_d also affects the resonant frequency and circuit impedance, the frequency locking mechanism in the coupled array ensures that all oscillator elements operate at a consistent common frequency, which suppresses frequency detuning and makes phase mismatch the dominant factor in the degradation of power combining efficiency [24].

In the equivalent circuit model, the equivalent resistance of the slot antenna remains constant, so the impedance shift caused by small C_d deviations is very limited. Meanwhile, the resulting change in oscillation amplitude is too slight to cause a measurable reduction in combining efficiency. Therefore, the observed power degradation can be primarily attributed to phase mismatch between oscillator units. Figure 9 illustrates the phase distribution of the 2 × 2 oscillator array. The phases of the diagonal units are maintained identical, i.e., $\theta_1 = \theta_4 = \theta_A$ and $\theta_2 = \theta_3 = \theta_B$. Accordingly, the phase difference between the two groups of oscillator units is defined as $\Delta\theta = |\theta_A - \theta_B|$. By sweeping $\Delta\theta$, the degradation of coherent power combining efficiency caused by phase mismatch can be quantitatively evaluated.

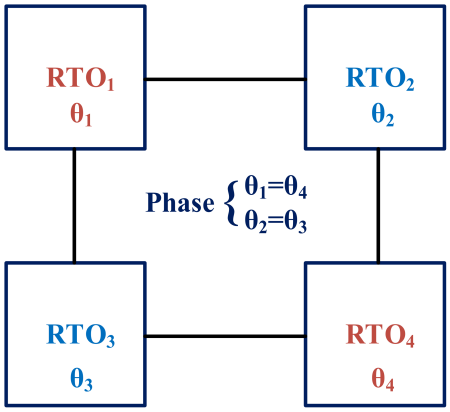


Figure 9. Phase schematic diagram of the 2 × 2 oscillator array units.

Figure 10 illustrates the relationship between active layer thickness, phase perturbation, and capacitance variation, where only the active-layer thickness is varied while all other parameters remain unchanged. By gradually varying the active-layer thickness to emulate fabrication-induced process variations, phase perturbations ranging from 0° to 2° are introduced among the array units. Active-layer thickness variation causes a C_d mismatch and, in turn, phase perturbation among the units. Taking C_d as the representative variable of fabrication-induced variation and holding the I–V characteristic, NDR, and resonant voltage fixed, the analysis focuses on this dominant channel to efficiency degradation, as minor amplitude changes are too small to explain the efficiency drop. Both the phase perturbation and capacitance variation exhibit an approximately linear increase with increasing active-layer thickness, demonstrating a strong correlation between capacitance variation and phase perturbation.

Figure 11 presents the simulated time-domain output waveforms of the 2 × 2 RTD oscillator array to demonstrate the influence of intrinsic capacitance mismatch on the phase evolution and waveform synchronization among oscillator units. By varying the intrinsic capacitance difference ΔC_d between adjacent oscillator units, the corresponding phase offsets $\Delta\theta$ are introduced. Specifically, when ΔC_d is set to 1 fF and 1.8 fF, the resulting phase offsets between oscillator units are 15° and 33°, respectively. This work adopts a selected, deterministic and symmetric phase configuration as a controlled parametric baseline. With the remaining circuit parameters held fixed, this setting is used to isolate the fundamental physical mechanism between capacitance mismatch, phase perturbation, and power combining efficiency; the resulting trend and relative sensitivity are examined under this controlled arrangement rather than over all possible random phase combinations. Considering the high computational cost, a statistical Monte Carlo analysis with randomized C_d variations is identified as a future direction to further enhance the practical relevance of the proposed model.

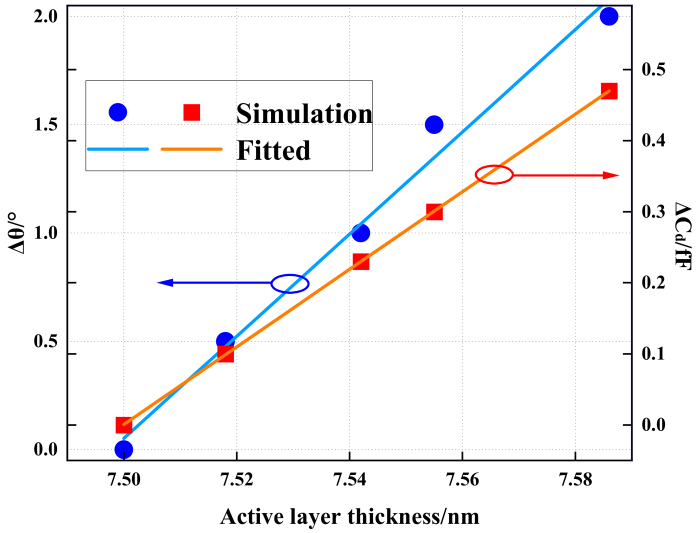


Figure 10. Relationship between active layer thickness, phase perturbation, and capacitance variation. The blue arrows indicate the trend of phase perturbation corresponding to the left y-axis, and the red arrows indicate the trend of capacitance variation corresponding to the right y-axis. The ellipses highlight the correlation between the fitted curves and the simulated data.

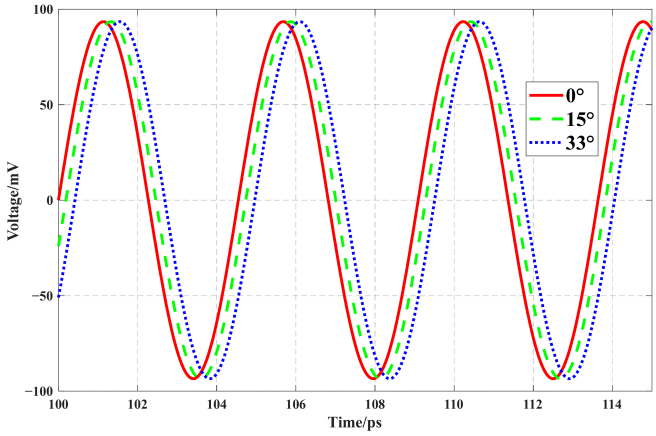


Figure 11. Time-domain output waveforms of the 2 × 2 oscillator array under different phase differences.

3.4. Effect of Phase Perturbation on Power Combining in the 2 × 2 Array

Using the capacitance-based phase-tuning strategy introduced in Section 3.3, the impact of small-magnitude phase perturbations on coherent power combining is quantitatively assessed for the 2 × 2 RTD oscillator array. Controllable phase differences between adjacent elements are introduced by adjusting the intrinsic capacitance of each oscillator unit, and the resulting degradations in output power and combining efficiency are quantified. In practical implementations, phase perturbations originate from fabrication-induced process variations among oscillator units; therefore, small phase perturbations are considered in this study. Figure 12 presents the output power characteristics of the 2 × 2 oscillator array under different phase differences among array elements, corresponding to phase perturbations of 0.5°, 1.0°, 1.5°, and 2.0°.

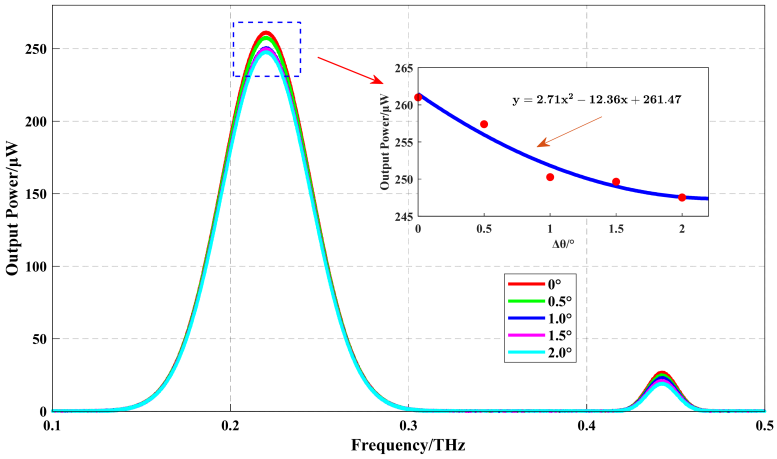


Figure 12. Output power curves of the 2 × 2 oscillator array under different inter-element phase differences. The red circles in the inset represent the simulated output power data.

The simulation results show that the RTD oscillator array achieves a maximum output power of 269.71 μW under the zero-phase-difference condition ($\Delta\theta = 0°$), corresponding to a power combining efficiency of 90.43%. As the phase difference among array units increases, both the output power and combining efficiency gradually decrease. When the phase difference increases to approximately 2°, the output power decreases from 269.71 to 255.32 μW, while the combining efficiency drops from 90.43% to 85.61%, a reduction of 4.82 percentage points. Furthermore, curve fitting analysis reveals a nonlinear dependence of the array output power on the phase difference, indicating the sensitivity of coherent power combining performance to phase mismatch.

To validate the effectiveness of the lumped approximation in capturing the degradation trend, a controlled comparison against a distributed transmission-line model was conducted. In this comparison, to accurately represent the distributed characteristics within the equivalent circuit, the original coupling interconnection was divided into two symmetrical segments. Each segment, with a physical length of approximately 90 μm, was replaced by an ideal transmission line model defined by a characteristic impedance of 50 Ω and a propagation delay of 0.474 ps, corresponding to an electrical length of about 37.5°. The total equivalent 38.6 Ω ohmic loss was maintained in series. The distributed model exhibits a relative power reduction of 5.46% under the same 2° perturbation, demonstrating a trend that is reasonably consistent with the 5.34% reduction observed in the lumped model. This minor deviation indicates that the lumped equivalent circuit is a valid approximation for capturing the phase-perturbation sensitivity. Furthermore, this lumped approach significantly simplifies the circuit topology, providing a computationally efficient framework for extending the analysis to larger configurations such as the 4 × 4 array. Consequently, this approximation provides a reliable and simplified framework for analyzing the impact of phase perturbations on power combining efficiency.

It should be noted that the simulated total power reduction of 14.39 μW is significantly larger than the ideal pure phase-cancellation estimate of approximately 0.03%. To quantitatively verify the power balance, this reduction is decomposed based on the equivalent circuit model. First, an extra ohmic loss of approximately 8.94 μW occurs in the coupling network due to phase-induced current redistribution. Second, since the phase perturbation is applied to one diagonal pair, only the two phase-shifted units experience extra nonlinear dissipation. The simulation indicates that the power consumed by the internal resistance R_d of each shifted unit increases by approximately 2.67 μW, resulting in a total additional nonlinear dissipation of 5.34 μW. This arises because the phase shift causes the AC voltage waveform to deviate from the ideal in-phase condition, and the nonlinear characteristics of

the voltage-controlled current sources G_1 and G_2 distort the tunneling current. The remaining fraction corresponds to pure phase cancellation, calculated to be approximately 0.04%, which is very close to the theoretical limit of about 0.03%. The slight deviation is naturally attributed to the inherent approximations of the equivalent circuit model. Consequently, this complete power balance confirms that the capacitance-induced phase perturbation modifies the nonlinear operating state of the coupled array, thereby increasing the dissipative losses. The additional ohmic and nonlinear dissipations are therefore direct physical consequences of this state alteration.

3.5. Effect of Phase Perturbation on Power Combining in the 4 × 4 Array

To further explore the scalability of the proposed array architecture, the phase-perturbation analysis is extended to the larger-scale 4 × 4 RTD oscillator array. Figure 13 first compares the phase difference Δθ versus the intrinsic capacitance difference ΔC_d between the 2 × 2 and 4 × 4 configurations. The simulation results obtained from the oscillator equivalent-circuit model show that, for the same capacitance variation, the phase difference of the 4 × 4 array is approximately 10% larger on average than that of the 2 × 2 array. However, when the capacitance difference increases to 3.2 fF or above, the phase responses of the two array configurations gradually approach each other, indicating a similar phase tuning behavior at larger capacitance variations. The enhanced phase sensitivity in the larger array originates from the increased number of coupled oscillator interactions, which amplifies the effect of intrinsic parameter variations on the collective phase state.

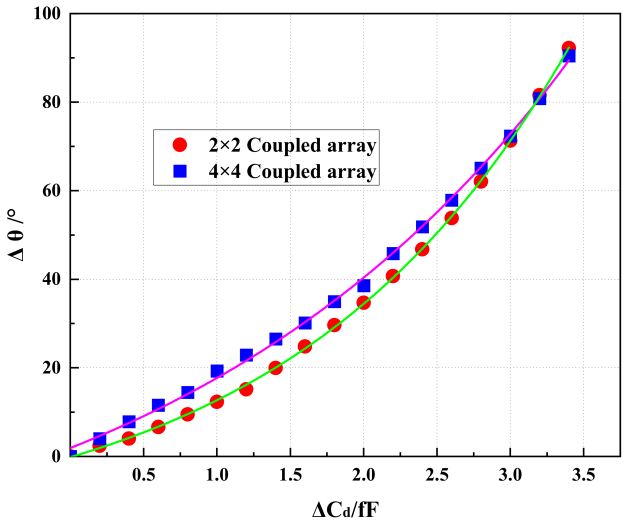


Figure 13. Phase tuning variation curves among different oscillator array scales. The red circles and red line represent the 2 × 2 coupled array, while the blue squares and blue line represent the 4 × 4 coupled array.

The output power characteristics of the 4 × 4 RTD oscillator array under different inter-element phase differences are investigated, as shown in Figure 14. The simulation results show that the maximum output power of 1053.39 μW is achieved under the zero-phase-difference condition (Δθ = 0°). When the phase difference increases to 2°, the output power decreases from 1053.39 to 1003.56 μW, while the combining efficiency drops from 88.30% to 84.12%, a reduction of 4.18 percentage points. Compared with the 2 × 2 array, the 4 × 4 array maintains a high power combining efficiency under small phase perturbations, demonstrating the scalability of the proposed array architecture for high-power THz sources.

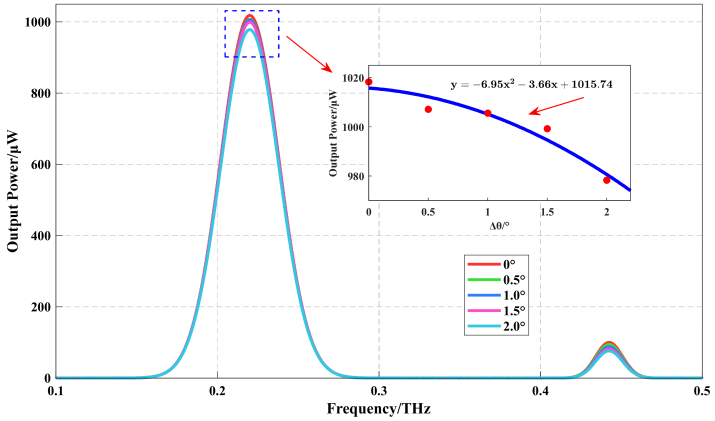


Figure 14. Output power curves of the 4 × 4 oscillator array under different inter-element phase differences. The red circles in the inset represent the simulated output power data.

4. Conclusions

In this work, an equivalent-circuit model of RTD oscillators based on two nonlinear voltage-controlled current sources is employed to investigate how fabrication-induced device variations affect phase synchronization and coherent power combining of terahertz RTD oscillator arrays. In the model, the resonant tunneling current and residual excess current of the RTD are represented by two nonlinear voltage-controlled current sources, while the slot antenna is characterized by an equivalent RLC resonant network. By introducing intrinsic capacitance variations among oscillator units, the model enables quantitative analysis of fabrication-induced phase perturbations and their impact on synchronization stability and power combining efficiency. Based on this model, a GaInAs/AlAs RTD oscillator unit operating at 220 GHz is analyzed. The simulated I–V characteristics agree well with experimental results, reproducing the negative differential resistance region. The oscillator unit achieves stable fundamental oscillation with an output power of 74.56 μW. Furthermore, 1 × 2 and 2 × 2 oscillator arrays are constructed using the proposed coupling configuration, achieving output powers of 140.67 μW and 269.71 μW with power combining efficiencies of 94.33% and 90.43%, respectively. The array structure is further extended to a 4 × 4 configuration, achieving an output power of 1053.39 μW and a combining efficiency of 88.30%, demonstrating the scalability of the proposed RTD oscillator array architecture. The influence of phase perturbations on coherent power combining performance is systematically investigated by adjusting the intrinsic capacitance difference among oscillator units. The results show that phase mismatch leads to nonlinear degradation of array output performance. For the 2 × 2 array, increasing the phase perturbation from 0° to 2° reduces the output power from 269.71 to 255.32 μW, while the combining efficiency drops from 90.43% to 85.61%, a degradation of 4.82 percentage points. The quantitative power balance analysis reveals that the capacitance-induced phase perturbation modifies the nonlinear operating state of the coupled array, thereby increasing the dissipative losses. The results provide quantitative insights into the relationship between fabrication-induced variations, phase perturbations, synchronization characteristics, and power combining efficiency. The proposed equivalent-circuit modeling approach offers an effective framework for optimizing phase control strategies and designing scalable, high-efficiency terahertz RTD oscillator arrays. In this equivalent-circuit modeling, the coupling network is represented by a lumped resistor as a simplification. The feasibility and reliability of this approximation have been verified through the controlled comparison with a distributed transmission-line model, supporting its application in analyzing the impact of fabrication-induced phase perturbations on combining efficiency. Furthermore, this simplified approach effectively reduces the

circuit complexity and facilitates the extension of the analysis to larger-scale arrays. Future work will focus on full-wave electromagnetic simulations to capture finer distributed effects and incorporate more comprehensive fabrication-variation models into array designs.

Author Contributions: Conceptualization, L.Y.; methodology, L.Y.; software, G.Y.; validation, G.Y.; formal analysis, G.Y.; investigation, G.Y.; resources, H.W.; data curation, G.Y.; writing—original draft preparation, L.Y. and G.Y.; writing—review and editing, L.Y. and G.Y.; visualization, G.Y.; supervision, L.Y., H.W., Y.L., S.Y. and H.Z.; project administration, L.Y. All authors have read and agreed to the published version of the manuscript.

Funding: This research was funded by the National Natural Science Foundation of China, grant number 62405219.

Data Availability Statement: The original contributions presented in the study are included in the article. Further inquiries can be directed to the corresponding author.

Conflicts of Interest: The authors declare no conflicts of interest.

Abbreviations

The following abbreviations are used in this manuscript:

RTD	Resonant tunneling diode
NDR	Negative differential resistance
THZ	Terahertz
PVCR	Peak-to-valley current ratio

References

1. Williams, S.L.; Reising, S.C. Design and Fabrication of Narrow-Band Waveguide Resonators near 380 GHz. *Electronics* **2026**, *15*, 4016. [CrossRef]
2. Ferguson, B.; Zhang, X.-C. Materials for terahertz science and technology. *Nat. Mater.* **2002**, *1*, 26–33. [CrossRef] [PubMed]
3. Thomas, S.; Virdi, J.S.; Babakhani, A.; Roberts, I.P. A Survey on Advancements in THz Technology for 6G: Systems, Circuits, Antennas, and Experiments. *IEEE Open J. Commun. Soc.* **2025**, *6*, 1998–2013. [CrossRef]
4. Asada, M.; Suzuki, S.; Kishimoto, N. Resonant Tunneling Diodes for Sub-Terahertz and Terahertz Oscillators. *Jpn. J. Appl. Phys.* **2008**, *47*, 4375–4384. [CrossRef]
5. Suzuki, S.; Teranishi, A.; Hinata, K.; Asada, M.; Sugiyama, H.; Yokoyama, H. Fundamental Oscillation of up to 831 GHz in GaInAs/AlAs Resonant Tunneling Diode. *Appl. Phys. Express* **2009**, *2*, 054501. [CrossRef]
6. Asada, M.; Suzuki, S. Resonant Tunneling Diodes for Room-Temperature Terahertz Oscillators. In Proceedings of the 2013 Asia-Pacific Microwave Conference (APMC), Seoul, Republic of Korea, 5–8 November 2013; pp. 1–3. [CrossRef]
7. Kasagi, K.; Suzuki, S.; Asada, M. Large-Scale Array of Resonant-Tunneling-Diode Terahertz Oscillators for High Output Power at 1 THz. *J. Appl. Phys.* **2019**, *125*, 151601. [CrossRef]
8. Suzuki, Y.; Mai, T.V.; Yu, X.; Suzuki, S.; Asada, M. Phase Control of Terahertz Waves Using Injection-Locked Resonant Tunneling Diode Oscillator. *IEEE Trans. Terahertz Sci. Technol.* **2022**, *12*, 481–488. [CrossRef]
9. Wang, C.; Yao, Y.; Jiang, H.; Xiu, T.; Syedd, M.A.S.; Yu, J.; Chen, X. Highly Integrated Resonant Tunneling Diode with Rectangular Waveguide Output for W-Band Communication System. *Electronics* **2020**, *9*, 485. [CrossRef]
10. Zhao, F.; Zhu, C.; Guo, W.; Cong, J.; Tee, C.A.T.H.; Song, L.; Zheng, Y. Resonant Tunneling Diode (RTD) Terahertz Active Transmission Line Oscillator with Graphene-Plasma Wave and Two Graphene Antennas. *Electronics* **2019**, *8*, 1164. [CrossRef]
11. Asada, M. Theoretical analysis of subharmonic injection locking in resonant-tunneling-diode terahertz oscillators. *Jpn. J. Appl. Phys.* **2020**, *59*, 018001. [CrossRef]
12. Meng, F.; Tang, Z.; Ourednik, P.; Hazarika, J.; Feiginov, M.; Suzuki, S.; Roskos, H.G. High-power even- and odd mode emission from linear arrays of resonant-tunneling-diode (RTD) oscillators in the 0.4- to 0.8-THz frequency range. *arXiv* **2024**, arXiv:2404.07394. [CrossRef]
13. Asada, M.; Suzuki, S. Terahertz Oscillators Using Electron Devices—An Approach with Resonant Tunneling Diodes. *IEICE Electron. Express* **2011**, *8*, 1110–1126. [CrossRef]
14. Schulman, J.N.; De Los Santos, H.J.; Chow, D.H. Physics-Based RTD Current-Voltage Equation. *IEEE Electron Device Lett.* **1996**, *17*, 220–222. [CrossRef]

15. Yang, Q.; Ren, Y.-F.; Shen, S.-M. Study of RTD's Equivalent Model and Its Application Circuits by Pspice. *Micronanoelectron. Technol.* **2008**, *45*, 131–135. [CrossRef]
16. Orihashi, N.; Hattori, S.; Suzuki, S.; Asada, M. Experimental and Theoretical Characteristics of Sub-Terahertz and Terahertz Oscillations of Resonant Tunneling Diodes Integrated with Slot Antennas. *Jpn. J. Appl. Phys.* **2005**, *44*, 7809–7815. [CrossRef]
17. Sheng, H.-Y.; Chua, S.-J.; Sinkkonen, J. Capacitance Property of a Resonant Tunneling Diode. *Mod. Phys. Lett. B* **1993**, *7*, 465–470. [CrossRef]
18. Asada, M.; Suzuki, S. Theoretical Analysis of Coupled Oscillator Array Using Resonant Tunneling Diodes in Subterahertz and Terahertz Range. *J. Appl. Phys.* **2008**, *103*, 124514. [CrossRef]
19. Mai, V.T.; Tran, T.T.H.; Nguyen, T.L.; Kieu, K.P.; Nguyen, T.H.; Pham, H.Y.; Luong, D.M. Terahertz Resistor-Coupled Arrayed Resonant-Tunneling-Diode Oscillators with High DC-to-RF Efficiency Using Metal-Insulator-Metal Capacitor. *Rev. J. Electron. Commun.* **2024**, *14*, 39–44. [CrossRef]
20. Sharifi, M.J.; Banadaki, Y.M. A SPICE Large Signal Model for Resonant Tunneling Diode and Its Applications. In *Proceedings of the Computational Methods in Science and Engineering, Athens, Greece, 16–20 September 2009*; Simos, T.E., Maroulis, G., Eds.; AIP: Melville, NY, USA, 2009; pp. 890–893. [CrossRef]
21. Suzuki, S.; Urayama, K.; Asada, M. Coherent Power Combination in Multi-Element Sub-Terahertz Resonant Tunneling Diode Oscillators Coupled with Metal–Insulator–Metal Stub Structure. *Appl. Phys. Express* **2008**, *1*, 093001. [CrossRef]
22. Okumura, N.; Asakawa, K.; Suhara, M. Analysis of Relaxation Oscillation in a Resonant Tunneling Diode Integrated with a Bow-Tie Antenna. *IEICE Trans. Electron.* **2017**, *E100-C*, 430–438. [CrossRef]
23. Han, F.; Shimura, T.; Tanaka, H.; Suzuki, S. Two Coupled Resonant-Tunneling-Diode Oscillators with an Air-Bridged Transmission Line for High-Power Coherent Terahertz Radiation. *Appl. Phys. Express* **2023**, *16*, 064003. [CrossRef]
24. Koyama, Y.; Kitazawa, Y.; Fujimoto, K.; Sato, T.; Iba, J.; Sakurai, K.; Ichikawa, T.; Yukimasa, K.; Uchida, T.; Yoshioka, T. A High-Power Terahertz Source Over 10 mW at 0.45 THz Using an Active Antenna Array With Integrated Patch Antennas and Resonant-Tunneling Diodes. *IEEE Trans. Terahertz Sci. Technol.* **2022**, *12*, 510–519. [CrossRef]

Disclaimer/Publisher's Note: The statements, opinions and data contained in all publications are solely those of the individual author(s) and contributor(s) and not of MDPI and/or the editor(s). MDPI and/or the editor(s) disclaim responsibility for any injury to people or property resulting from any ideas, methods, instructions or products referred to in the content.